Experimental investigation of the mechanical stiffness of periodic framework-patterned elastomers*

N. Francois, T. Arnoux, L. Garcia, S.T. Hyde, V. Robins,
M. Saadatfar, M. Saba[1], and T.J. Senden.
Department of Applied Mathematics, Research School of Physics and Engineering,
The Australian National University, Canberra ACT 0200.
[1] Institut für Theoretische Physik I,
Friedrich-Alexander Universität Erlangen-Nürnberg,
Germany

May 10, 2013

Abstract

Recent advances in the cataloguing of 3d nets mean a systematic search for framework structures with specific properties is now feasible. Theoretical arguments about the elastic deformation of frameworks suggest characteristics of mechanically isotropic networks. We explore these concepts on both isotropic and anisotropic networks by manufacturing porous elastomers with three different periodic net geometries. The blocks of patterned elastomers are subjected to a range of mechanical tests to determine the dependence of elastic moduli on geometric and topological parameters. We report results from axial compression experiments, three-dimensional x-ray CT imaging, and image-based finite-element simulations of elastic properties of framework-patterned elastomers.

1 Introduction

Surveys of natural and manufactured materials show a significant gap in the low density ($\rho < 500$ kg/m^3), high Young's modulus ($E > 1GPa$) range [1]; materials with high Young's modulus (e.g. solid metal alloys) tend to have high density. An elegant route to low density materials is to form porous materials, whose solid phase is itself intrinsically stiff. Hashin and Shtrikman (H-S) have derived theoretical upper bounds for elastic moduli of composite materials as a function of volume fraction and moduli of the bulk matrix [2], but the design of porous materials whose stiffness approaches those bounds remains a challenge.

A common manufacturing technique for porous materials is to create a foam. However, foams tend to have significantly lower Young's modulus than the bulk material, well below the H-S bounds. An alternative route to porous materials is to form framework materials, whose designs are based on periodic nets. In this paper we explore the elastic behaviour of frameworks both in theory and practice as a function of the

*To appear in Philosophical Transactions of the Royal Society A, 2013.

net geometry. We are particularly interested in net designs that resist deformation regardless of the direction of the imposed stress, i.e. materially isotropic and stiff porous elastomeric nets, as well as comparison of isotropic with anisotropic nets.

A key observation driving the design of framework materials is that a solid beam of linear-elastic material is much stiffer under axial stress than under bending. Since we can model a framework as an assembly of narrow beams (centred by net edges) meeting at junctions (net vertices), such a solid will be maximally stiff if it carries stress through axial deformation of these beams rather than bending. The question now is what structures have this property? Open-cell foams, for instance, can be considered as random frameworks made of beams that are polydisperse in size, but they usually show bending dominated behaviour [3]. Here we consider only ordered (crystalline) net geometries.

Deshpande *et. al* [4] argue that frameworks based on combinatorially rigid nets (in the sense of Maxwell constraint counting) carry stresses axially along the beams and will therefore show stretch-dominated behaviour. Frameworks based on under-constrained nets which have floppy modes (or mechanisms), will carry stresses in the junctions or through bending of their beams and should therefore have smaller moduli. In 2d these two cases are exemplified by the triangular lattice, **hxl** (rigid, stretch-dominated), and the honeycomb **hcb** (floppy, bending-dominated).*

The Maxwell-Calladine [7] rule for a general pin-jointed 3d framework with b bars and j joints is that the number of infinitesimal internal mechanisms m and states of self stress, s, satisfy:

$$b - 3j + 6 = s - m \tag{1.1}$$

If the framework has $m = s = 0$ then it is said to be *isostatic*; there are no moving joints and no redundant bars. For large homogeneous random frameworks this leads to a necessary condition on the average number of bars meeting at each joint, $\overline{z}$, (i.e. the vertex degree) that $\overline{z} \geq 6$. On the other hand, in [4] it is argued that a 3d periodic net with 'similarly situated nodes' must have $z \geq 12$. For other periodic and symmetric nets the conditions for combinatorial rigidity are still being explored [8, 9], but there is a possibility here for rigid nets with $6 \leq z \leq 12$.

Thus, in 3d the simplest rigid net is the face-centred cubic lattice **fcu** and frameworks with this topology have been analysed in depth [10]. The **fcu** framework is materially anisotropic, with different elastic moduli along different directions. The geometric constraints necessary to realise elastically isotropic framework materials with cubic symmetry is explored in detail by Durand and Gurtner [11]. Their analysis of the linear-elastic stress-strain equations leads to explicit geometric conditions for isotropic, stretch-dominated (affine) strain of a framework solid which are discussed further in Section 2, as well as estimates of the elastic moduli of isotropic framework materials that, to our knowledge, have yet to be explored experimentally.

The design of new micro-structured materials requires both a comprehensive dictionary of potential target structures and a reasonable process for building them. Systematic catalogues of periodic nets have arisen largely in structural chemistry. Examples are nets derived from uni-nodal sphere packings [12], O'Keeffe's *RCSR* database of

*We describe nets by a **boldface** three-letter code developed for chemical frameworks. Structural details for these nets can be found in the *RCSR* database at `rcsr.anu.edu.au` [5]. Patterned porous materials whose channels lie on net edges are denoted by the epinet code, *italicised*; see the *EPINET* database `epinet.anu.edu.au` [6].

nets most relevant to crystal chemistry [5], real and hypothetical zeolites [13, 14], and *EPINET* [6], a more general database that has the broadest range of topological parameters. For the engineer, these are new resources for exploring the dependence of material properties on geometric and topological framework parameters.

We have systematically explored the most symmetric net geometries listed in the *EPINET* (and *RCSR*) databases, to determine the simplest possible stretch-dominated porous networks. Guided by this theoretical analysis, we have manufactured patterned elastomeric materials based on some of those nets. We describe the experimental measurement of elastic moduli from sample frameworks and compare these measurements with x-ray CT image-based FEM numerical calculations.

2 Systematic search for isotropic stretch-dominated frameworks

The criteria derived in [11] for elastically isotropic frameworks that exhibit affine strain provide a natural starting point for our search, since these will select designs for lightweight stiff materials regardless of the loading geometry. Driven by recent advances in tiling theory that allow systematic enumeration of net geometries, ordered by their complexity [15, 16], we are now in a position to search for novel templates in a rational fashion. We have therefore analysed the simplest structurally isotropic nets — i.e. those with cubic symmetry — from the *EPINET* and *RCSR* databases. Nets with lower symmetry considerably complicate the analysis. Our list comprises 74 nets and includes all cubic nets whose vertices are symmetrically equivalent and contain up to two symmetrically distinct edges (i.e. {vertex,edge} transitivity {1,1} and {1,2}, with 19 and 30 nets respectively) and cubic nets with two symmetrically distinct vertices and a single edge type (transitivity {2,1}, 25 nets). We have sorted these nets according to their crystal classes, to determine whether elastic features are related to crystal class.[†] Results are collated in the Appendix.

Porous network materials can be considered as collections of elastic beams (centred by net edges) meeting at nodes (net vertices). Durand and Gurtner's analysis [17, 11] led to a suite of equations that a network should satisfy to exhibit affine stretch-dominated strain assuming no vertex contribution to the elasticity and standard beam elasticity theory. (This assumption holds in practice if the edge radii are much smaller than their lengths.) Adapting their notation in [11], denote by $\mathbf{e_i}$ an edge vector and $\widehat{\mathbf{e_i}}$ the unit edge vector. Denote by ℓ_i, a_i and v_i the length, cross-sectional areas and volumes of edges $\mathbf{e_i}$. The direction cosines of the edges with (Cartesian) coordinate axes are:

$$\{\cos(\theta_i^x), \cos(\theta_i^y), \cos(\theta_i^z)\} = \{\widehat{\mathbf{e_i}} \cdot \{1,0,0\}, \widehat{\mathbf{e_i}} \cdot \{0,1,0\}, \widehat{\mathbf{e_i}} \cdot \{0,0,1\}\}. \tag{2.2}$$

Denote the average measure of a variable q as the weighted average (by edge volume, v_i):

$$< q >:= \frac{\Sigma_i v_i q_i}{\Sigma_i v_i} = \frac{\Sigma_i a_i \ell_i q_i}{\Sigma_i a_i \ell_i}. \tag{2.3}$$

This average is made by summing over all edges within a single translational unit cell of the net.

[†]Of the five cubic classes, the class 23 is not represented in this selection.

Four additional sets of equations characterise materially isotropic nets that deform by stretching of the beams without bending (i.e. with axial strains). The derivation imposes a carefully chosen displacement field that ensures each (possibly curved) beam will deform affinely. The first set of equations are:

$$< \cos^2(\theta^\alpha) > \;=\; \frac{1}{3} \tag{2.4}$$

$$< \cos^4(\theta^\alpha) > \;=\; \frac{1}{5} \tag{2.5}$$

$$< \cos^2(\theta^\alpha)\cos^2(\theta^\beta)\cos^2(\theta^\gamma) > \;=\; 0 \tag{2.6}$$

Note that the first two equations have three separate components each ($\alpha = x, y, z$). The last equation has nine components, corresponding to permutations of α, β and γ, where ($\beta \neq \gamma$) [11]. For convenience, in the following discussion, we refer to net designs that satisfy these equations as (elastically) isotropic. Lastly, Durand and Gurtner derive an equation for mechanical equilibrium at the joints:

$$\Sigma_i a_i \cos(\theta_i^\alpha).\cos(\theta_i^\beta).\cos(\theta_i^\gamma) = 0 \tag{2.7}$$

for α, β and $\gamma = x, y$ or z. This equation contains ten separate equations. Where the sum over all edges emanating from a single vertex vanishes, we refer to the net as being at vertex-equilibrium.

We have calculated the sums given by the LHS of these four sets of equations for the list of 74 cubic nets described above. The results are summarised in Tables 3 and 4 in the Appendix. We do not find any clear correlation between cubic crystal class (point group symmetry) and elastic behaviour. Most examples are neither elastically isotropic nor at vertex-equilibrium. Indeed, all {1,1} and {2,1} transitive nets (i.e. with one type of edge) fail the isotropy conditions, since the summands of equations (2.4–2.7) do not give the required values. Therefore crystalline isotropic and stiff network materials must contain at least two symmetrically distinct classes of beams, corresponding to the distinct edges. In that case, the ratio of beam radii for the different edge classes can be tuned to satisfy the isotropy and vertex equilibrium equations.

Just two cubic net geometries from the 30 {1,2} transitive nets lead to sums that are exactly those demanded by the equations above for specific ratios of beam radii. These are the *sqc38* and *sqc1649* examples, with 14 (6 of one type, and 8 of the other) and 8 (6 and 2) edges meeting at each vertex respectively. The isotropy of the *sqc38* pattern has been reported earlier by Durand and Gurtner [11]; the second example is new. These nets are illustrated in Figure 1. They define frameworks that are elastically isotropic with stretch-dominated strains provided their cross-sectional area ratios are tuned as listed in Table 3.

3 Manufacture of elastomeric nets

The manufacture of patterned elastomers is now possible using 3d modelling software and rapid prototyping (3d printing) technology. We have therefore manufactured real materials based on some cubic net geometries to compare their elastic responses and test the validity of the analyses in the previous section. We have built models of various porosity based on the nets *sqc1* (**pcu**), *sqc3* (**bcu**) and *sqc38* (**sod-d**), see Fig. 3. The first two nets are anisotropic and not combinatorially rigid, but they are well-known

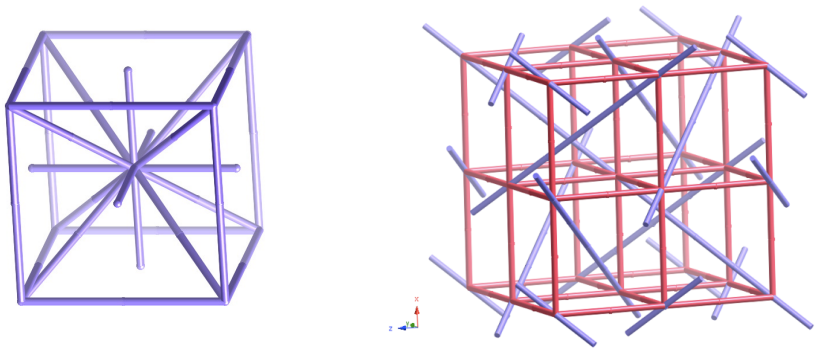

Figure 1: The nets *sqc*38 and *sqc*1649. These nets define the skeleta of porous framework geometries that can be tuned to be elastically isotropic, provided the edges are thickened to give circular beams. The radii of beams along the [100] and [111] directions (axial and diagonal directions) *must be tuned* to a specific ratio to form the optimal materials (see Table 3).

cubic 3d patterns — simple (or primitive) and body centred cubic nets. The third pattern, *sqc38*, is effectively the union of the first two. For a suitable choice of edge-radii, it will satisfy Durand's isotropy conditions, and it is combinatorially rigid (in fact it is over-constrained). Since the manufacturing process described here is a new technique, this initial experimental investigation is restricted to networks with uniform edge radii.

Direct printing of porous geometries is readily done, however the bulk material is typically a weakly consolidated granular solid, poorly suited for testing elastic properties of framework materials. (In our case, the printed material is made of consolidated gypsum powder, whose constituent particles are typically ca. 1μm in diameter.) To form a suitable porous material, we first print a complementary gypsum mould, which we then fill with liquid polymer polyvinylsiloxane (PVS) to create a block of framework-patterned elastomer. The physical constraints on the mould are the 3d printer resolution of 100 microns, and an effective casting limit on the minimum beam diameter of 1 millimeter. We construct models that are 6.6cm along an edge, with 9^3 repeat units of the basic pattern as follows.

Given a target lattice structure described by crystallographic data (as in *EPINET*), we create a computer model of the framework by generating 9^3 unit cells of the structure, then thickening all edges to have equal circular cross sections (whose radius is determined by the target porosity) and smoothing the nodes (see Fig. 2). A 3d digital model of the complementary volume, containing all points in the 6.6cm cube that are not in the framework is then formed. This is the mould geometry. The mould is then built in a Zprinter 650 machine using monodisperse gypsum powder, glued to form a consolidated monolith within the complementary volume. The resulting mould is typically filled with unconsolidated powder, which is removed carefully using a brush and an air-gun.

The resulting porous monolith is then saturated with ethylene glycol to prevent wetting by PVS. The PVS is then imbibed into the pore spaces, under pressure to give uniform, almost bubble-free filling, and subsequently air-cured to form the polymerised

elastomer. Lastly, the gypsum-PVS composite is washed in water to remove the gypsum mould, leaving the patterned elastomer, see Figs 2 and 4. Defects can occur during the process, due to the printing process and the presence of bubbles, but they usually represent a negligible part of the global structure. (The discrepancy between the target volume fraction and its actual realisation is within 1%.) The surface roughness of the beams is usually the main source of defects as can be noticed in Fig. 7.

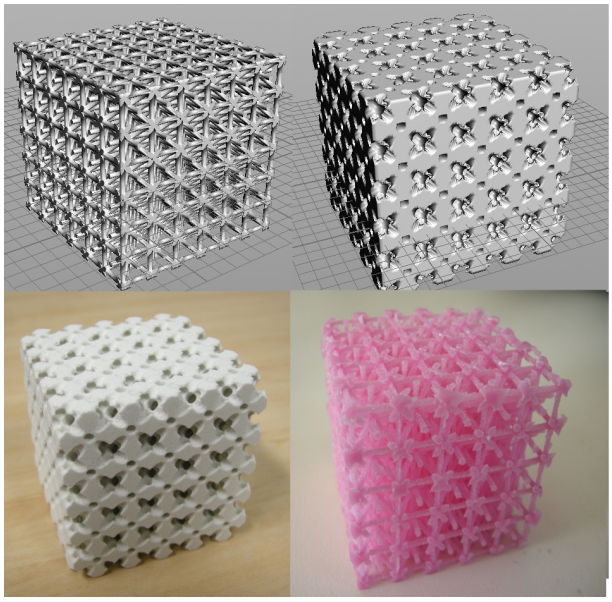

Figure 2: Clockwise from top left: An example of the computer model net geometry for *sqc38* and its complement, the PVS cast elastomer, and the gypsum mould as built in a Zprinter 650 machine.

4 Experimental investigation of elastomeric nets

Given a block of patterned PVS, cast as described above, we investigate its elastic properties with an axial compression apparatus (Instron). We also study the material deformation behaviour in three dimensions under uniaxial loading, using CT images of the material under various loading conditions.

The applied axial force and resulting displacement are measured using an Instron machine. The resolution of force and displacement measurements are $10^{-4}N$ and $10^{-7}m$ respectively. Data are shown in Fig. 5. When axially loaded along the z-axis direction (defined in Fig. 3), we see that in the linear-elastic regime *sqc1* has the stiffest response to compression, followed by *sqc38*, then *sqc3*. The data show a sharp onset of buckling in the *sqc1* patterned block of PVS followed by post-yield softening. The *sqc38* block yields at a similar level of compression ($d = 9$mm) as *sqc1* and thereafter the force changes little for increased deformation. Finally, *sqc3* shows a consistent linear response for the full deformation range studied ($0 < d < 21$mm).

We calculate Young's modulus under axial loading, E_z, from the compression measurements by finding the slope, s, of the line that best fits the data in the linear-response

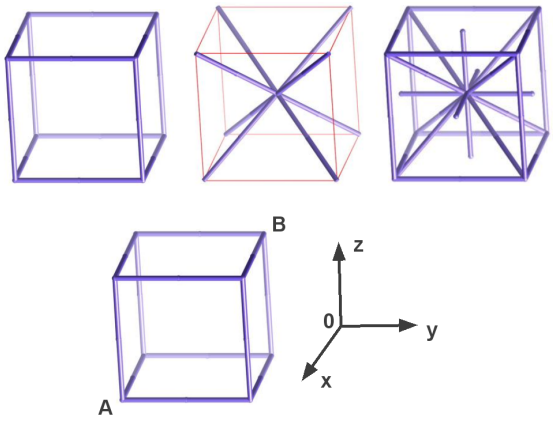

Figure 3: The nets used as templates for building the porous PVS networks discussed in this paper. From left to right: *sqc1* (simple cubic), with vertex degree $z = 6$, *sqc3* (body-centred cubic) $z = 8$, and *sqc38* with $z = 14$. The diagram below shows the orientation of axes referred to in the text.

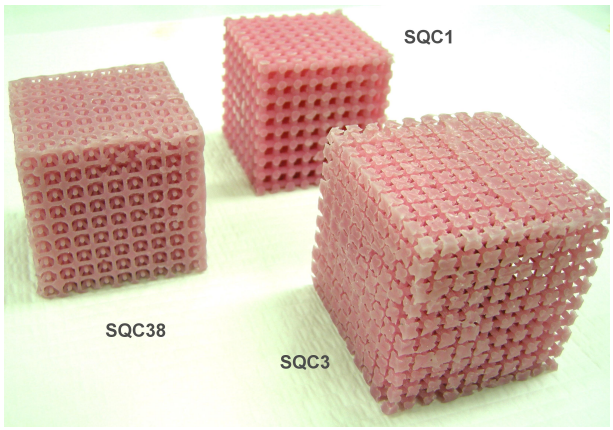

Figure 4: Examples of patterned blocks of PVS. Clockwise from left: *sqc38*, *sqc1* and *sqc3*.

region. Then for s in units N/m, and l, the block side length in meters, we have $E = s/l$ (Pa). See Table 1 for a summary of the results.

Uniaxial deformation measurements on *sqc1* and *sqc38* networks have been made for a range of axis orientations. To do those measurements, we manufactured a number of PVS patterned materials with equal underlying net geometries and porosities (i.e. **sqc1** and **sqc38**), all bounded externally by cube faces, and various orientations. Those models were then deformed, giving the experimental Youngs moduli plotted in Figure 6. The orientations of the cubic blocks are as follows. The initial orientation (state 0), with cube edges aligned with the axis of deformation (Fig. 4) is denoted $\theta 0$. $\theta 1$ describes the rotated structure whose new z deformation axis is parallel to the body diagonal of state 0 (AB in Fig. 3). $\theta 2$ refers to the body formed by rotating state 0 35.2° around the y axis and $\theta 3$ is the body formed by rotating state 0 45° around the y axis.

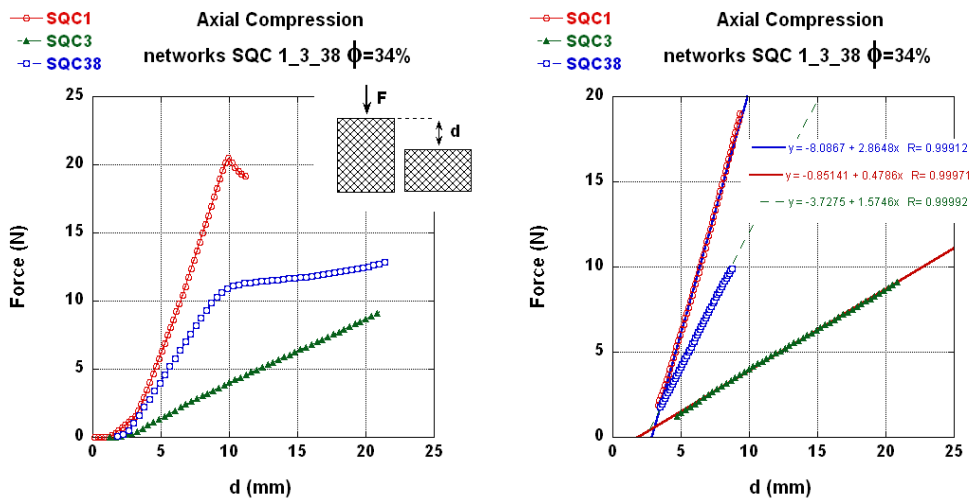

(a) (b)

Figure 5: (a) Force vs. displacement curves for axial compression of three blocks of patterned PVS. Each block has a volume fraction of $\phi = 0.34$. (b) Close-up view of linear region of plot in (a) with linear fits.

Table 1: Data used to calculate Young's modulus for three blocks of patterned elastomer based on *sqc1*, *sqc3*, and *sqc38* frameworks with volume fraction $\phi = 0.34$.

	Line of best fit slope, s (N/mm)	Block side length, l (cm)	Young's modulus E_z (kPa)
sqc1	2.86	6.60	43.4
sqc3	0.479	7.05	6.79
sqc38	1.57	6.60	23.9

In order to explore the geometric deformation modes of these networks, we have also imaged the patterned PVS materials using high resolution (65 microns) X-ray computerised tomography (XCT). We use a helical tomography apparatus that is capable of high resolution with a large imaging field of view [18]. The helical feature of our XCT is especially suitable for our specimens as it allows three-dimensional imaging of the complete sample under loading, including the compressing piston at the top of the sample.

The PVS block is placed inside a uniaxial compression cell [19], designed with a rigid piston, to load the top face of the patterned materials uniformly along the z-axis. The strain is varied by adding suitable weights to the loading piston. This entire ensemble is placed in the XCT machine and imaged with 2880 2D x-ray projections in 360°. The total image acquisition time was 5 hours for each stage of compression and tomographic reconstruction was made using the Katsevich algorithm [20]. The result is a 2048^3 three-dimensional voxel array with each voxel representing 65 microns resolution. For example a reconstructed image of *sqc38* with no loading is given in Fig. 7. These three-dimensional data contain a wealth of information. For example, we can extract medial

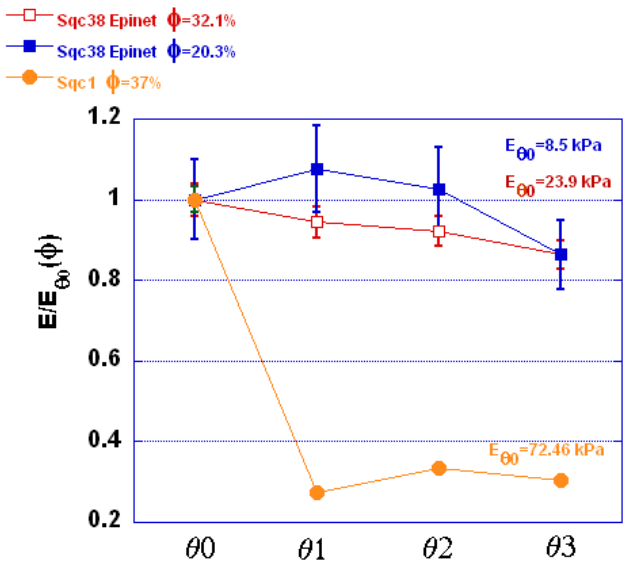

Figure 6: Youngs modulus measured under uniaxial compression for different body orientation and different geometry normalised by the modulus measured in state 0. The patterns are *sqc1* and *sqc38* with all edge-radii equal. The various orientations are described in the text.

axes from the volume data using numerical tools developed in-house [21], that allow precise quantification of the network edge and vertex geometry as a function of load. For the purposes of this paper, we use these three-dimensional data to build digital models of our patterned materials from which we numerically estimate their elastic moduli.

5 Image-based computation of elastic moduli

One advantage of tomographic imaging is that it permits direct simulation of an object's mechanical properties using a finite element method (FEM) [22, 23, 24]. First the x-ray density map of the tomographic image is *binarised*: based on the x-ray density value each voxel is assigned to be either PVS (i.e. part of the framework) or air. The voxels are then taken to be tri-linear cubical finite elements[22]. In order to calculate the mechanical response of the PVS framework, a constant strain (or displacement field) is initially applied across all the voxels. For anisotropic materials, we run six independent FE simulations to solve for the deformation field of six different applied external orthogonal strains: $\{xx, yy, zz, yz, xy, zx\}$. This way, we can construct any particular applied macroscopic strain as a combination of the selected strain basis producing sufficient data to calculate all 36 components (Voigt notation) of the sample's elastic stiffness tensor (C_{ijkl}).

Initial bulk and shear moduli of 850 and 139 KPa (Young's modulus of 395 KPa) were assigned to the solid phase (PVS)[‡] and a constant strain boundary condition

[‡]We measured these values using the Instron apparatus on a solid block of PVS that had undergone

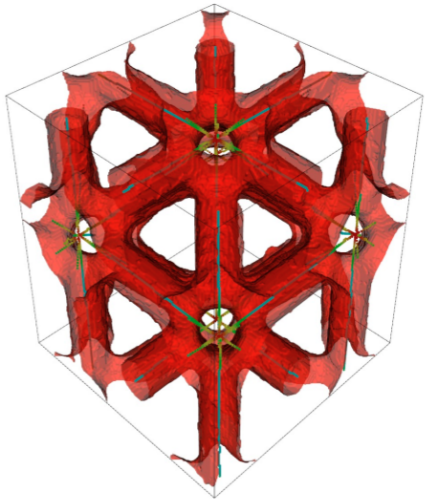

Figure 7: A 3D rendering of a tomographic image of *sqc38*. The translucent red surface is an isosurface of the x-ray density chosen to highlight the edges in the framework. The thin struts are the medial axis corresponding to the PVS phase.

scheme was used in the simulations [25]. The final elastic result (displacement distribution) is such that the total elastic energy ($\mathcal{E}$) stored in the microstructure is minimised:

$$\mathcal{E} = \frac{1}{2}\int_v \epsilon_{ij}\ C_{ijkl}\ \epsilon_{kl}\ dv \tag{5.8}$$

Here, ϵ is the strain field (a 2^{nd} rank tensor), C is the stiffness tensor (a 4^{th} rank tensor), dv is the volume element and the integration is over the entire sample. Minimisation of elastic energy means that the gradient of the energy with respect to elastic displacement variables, u_m, is zero ($\frac{\partial \mathcal{E}}{\partial u_m} = 0$). The FEM simulation outputs the full tensorial stress response of the PVS frameworks from which we compare the compressive axial element of the Young's moduls (E_z) with the experimental results in Fig. 8 and Table 2. There is good agreement between the values obtained by simulation and those from the Instron experiments for both the *sqc1* and *sqc38* blocks. Our experimental finding —that *sqc1* is stiffer under axial loading parallel to edge directions than *sqc38* loaded off-axis to edge directions— is reproduced by simulations. Normalised values of all three axial components of Young's modulus and shear moduli for *sqc1* and *sqc38* blocks are presented in Fig. 9. At the initial loading stage, when the force is sufficiently low that the block deforms as a linear-elastic body (determined by the Instron data), we see that the *sqc1* framework has $E_z/E_{PVS} = 0.22$ and $E_y/E_{PVS} = E_x/E_{PVS} = 0.10$, where E_z and E_y denote moduli parallel and orthogonal to the loading axis respectively. With increased loading in the z-axis, E_z maintains this value, while the other two components increase to around the same level. The shear moduli for the *sqc1* block have also been estimated from the FEM simulations by imposition of uniform strains in xz, yz and xy planes as described earlier. These moduli too show qualitatively different behaviour between the initial and final loading stages. The initial configuration has one shear

the same curing process as the elastomeric nets.

component much larger than the other two — relative values of 0.26 vs 0.10 — with the large component representing a shear in the plane of the slight axial compression while the other two components are in the transverse plane. This distinction disappears at the higher loading configurations so that all three components are around 0.10 to 0.11. In contrast, the moduli computed from images of the *sqc38* block are quite consistent at the different loading stages. All three components for Young's modulus increase slightly from an initial relative value of 0.11 to a final value of 0.14. The two transverse components of the shear modulus sit at around 0.14 while the third component increases slightly from 0.17 to 0.19.

Table 2: Summary of the elastic properties of *sqc1* and *sqc38* framework patterned blocks of PVS. The Young's moduli from the Instron experiment are calculated from the full linear regime, for the simulation we report values from the initial loading stage.

	Young's modulus (Y_z) from experiment [kPa]	Young's modulus (Y_z) from simulation [kPa]
sqc1	43.4	44 ± 0.87
sqc38	23.9	25 ± 0.91

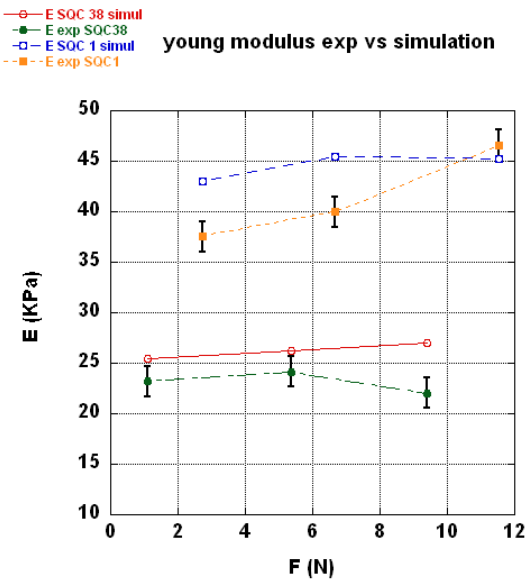

Figure 8: Young's modulus vs force. Graphical comparison of the z-axial Young's modulus as computed from Instron axial compression data and from FEM analysis of xct images of the same models under three different loading conditions. These loadings are within the linear elastic regime found with the Instron experiments Fig. 5.

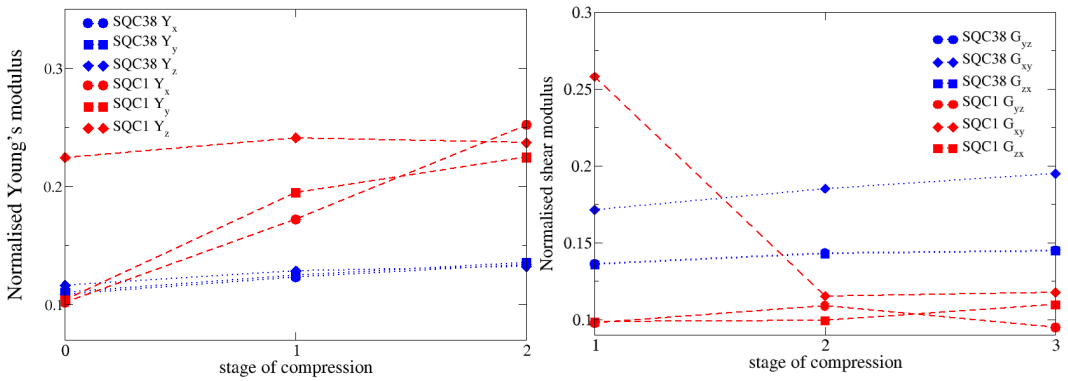

Figure 9: Axial components of Young's modulus (*left*) and shear modulus (*right*) for *sqc1* (red dashed line) and *sqc38* (blue dotted line) patterned blocks of PVS normalised by modulii for a solid block of PVS. The values are computed from FEM analysis of xct images of the blocks under three different loading conditions.

6 Discussion of results

Recall that our theoretical survey of cubic nets with symmetrically equivalent vertices suggests just two patterns with up to two symmetrically distinct edges, according to the criteria deduced by Durand et al. [11]. One of those, *sqc38*, is predicted to be isotropic when the ratio of cross-sectional area between the two edge types is ≈ 0.77 (*cf.* Table 3). Our *sqc38* patterned material, with an edge ratio of 1.0, is therefore expected to be nearly isotropic. That expectation is confirmed by the measurements of stiffness for various loading orientations, both on- and off-axis relative to edge directions, as shown in Figure 6. The axial Young's modulus of *sqc38* varies by around 10%, confirming a largely isotropic response, as shown in Fig. 6.

In contrast, axial compression of *sqc1* patterned materials display a reduction in the axial Young's modulus by 70% when the orientation of the pattern with respect to the cast block changes from being aligned with the cubic edges to other non-aligned directions. Evidently, this material is far from isotropic.

Nevertheless, axial compression results in Section 4, Fig. 5 show that the *sqc1* block is stiffer when strained along the z-axis direction than the *sqc38* block with equivalent porosity, despite the fact that *sqc38* is combinatorially rigid, while *sqc1* is not. This is an instructive result, that belies a simple correspondence between rigid and stiff structures. Although *sqc1* is not combinatorially rigid, whereas *sqc38* is, it is nevertheless relatively stiff. That stiffness, is in part due to the fact that the *sqc1* patterned elastomer was built with a larger edge radius (1.69 mm vs 0.75 mm) to maintain equal porosities for both materials. Perhaps more significantly, the axial compression occurs along an edge direction of the *sqc1* material, so the framework deforms by compression rather than bending. In contrast, the edges of the rigid body-centred cubic framework *sqc3* lie along body diagonals of cubic unit cell, so z-axial compression of the block is bending- rather than stretching-dominated. The *sqc38* material shows intermediate stiffness to *sqc1* and *sqc3* under uniaxial strain parallel to the z-axis of the cubic unit cell common to all three patterns. Indeed, the axial Young's modulus for *sqc3* is considerably lower than that for *sqc38* (7.5kPa vs 24 kPa) despite the fact that the *sqc3* block has framework edges that

are thicker than those for *sqc38* (1.1 mm vs 0.75mm). This too is consistent with the relative stiffness of edges under compression along the z-axis compared with bending. *sqc1* deforms by edge compression only, *sqc38* via a combination of compression (for the edges that are also found in the *sqc1* pattern) and bending (for other edges) and the *sqc3* deformation is dominated by bending.

Results from image-based FEM simulations in Section 5 confirm (see Fig. 8) and extend the conclusions deduced from Instron data. In particular, the simulations at all three loading stages (seef Fig. 9) are consistent with quasi-isotropic behaviour in the axial and shear moduli computed from the *sqc38* images .

It is interesting to note that the transverse components of Young's modulus (E_x, E_y) and one shear component of the *sqc1* network change considerably as the loading increases, however. This hints at a much more complex deformation process for the *sqc1* patterned elastomer, confirmed visually by anisotropic buckling of the material at higher loading. A quantitative study of the structural deformation of these frameworks from the XCT images will be included in a future paper.

To obtain a better picture of how elastic properties depend on the underlying net structure, we need to consider the moduli as a function of porosity. Durand and Gurtner [17] derive expressions for elastic constants of nets that satisfy their isotropy stretch-dominated strain conditions and argue that Young's modulus scales as $E = (\phi/6)E_0$, where E_0 is Young's modulus for the bulk material. They also observe that this is strictly lower than the bounds implied by Hashin-Shtrikman for general composite materials. Our block of *sqc38*-patterned PVS does not quite fulfill their criteria since we have made all edge radii the same. Nevertheless, taking a value of $E_0 = 395$ kPa as per the FEM simulations, we see that their theory predicts $E = 22.4$ kPa, which is consistent with, although slightly lower than, the experimental determination of 24 kPa. The source of this discrepancy may be traced to a number of factors, from structural defects in our elastomeric models, to approximations in Durand and Gurtner's theory (that assume thin beams and neglect vertex contributions to the elasticity). A more detailed analysis of Young's modulus as a function of porosity for a given framework type will be given in the follow-up paper.

In conclusion, the simple distinction between the stiffness of rigid (stretch-dominated) structures and non-rigid (bending-dominated) structures does not hold for our blocks of framework-patterned elastomers. Our experiments demonstrate the fact that non-rigid, anisotropic structures may be stiffer than rigid isotropic ones along certain axes. Further, a second candidate for isotropic stiff patterns, *sqc1649* is identified from the epinet database. Clearly, there is plenty of scope for further experiments and analysis, and the search for light-weight stiff and strong materials continues.

References

[1] M.F. Ashby. *Materials selection in mechanical design*. Butterworth-Heinemann, Burlington, MA, USA, 4th ed. edition, 2011.

[2] Z. Hashin and S. Shtrikman. A variational approach to the theory of the elastic behaviour of multiphase materials. *Journal of the Mechanics and Physics of Solids*, 11(2):127 – 140, 1963.

[3] M.F. Ashby. The properties of foams and lattices. *Phil. Trans. R. Soc. A*, 364:15–30, 2006.

[4] V.S. Deshpande, M.F. Ashby, and N.A. Fleck. Foam topology bending versus stretching dominated architectures. *Acta materialia*, 49:1035–1040, 2001.

[5] M. O'Keeffe, M. A. Peskov, S. Ramsden, and O. M.Yaghi. RCSR: Reticular Chemistry Structural Resource. `http://rcsr.anu.edu.au`.

[6] Stephen Hyde, Vanessa Robins, and Stuart Ramsden. Epinet. `http://epinet.anu.edu.au`, 2008.

[7] C.R. Calladine. Buckminster Fuller's 'tensegrity' structures and Clerk Maxwell's rules for the construction of stiff frames. *International Journal of Solids and Structures*, 14:161–172, 1978.

[8] S.D Guest and J.W Hutchinson. On the determinacy of repetitive structures. *Journal of the Mechanics and Physics of Solids*, 51(3):383 – 391, 2003.

[9] P.W. Fowler and S.D. Guest. A symmetry extension of maxwell's rule for rigidity of frames. *International Journal of Solids and Structures*, 37(12):1793 – 1804, 2000.

[10] V.S. Deshpande, N.A. Fleck, and M.F. Ashby. Effective properties of the octet-truss lattice material. *Journal of the Mechanics and Physics of Solids*, 49:1747–1769, 2001.

[11] G. Gurtner and M. Durand. Structural properties of stiff elastic networks. *Europhysics Letters*, 87:24001, 2009.

[12] E. Koch and W. Fischer. Types of sphere packings for crystallographic point groups, rod groups and layer groups. *Z. Krist.*, 148:107–152, 1978.

[13] Ch. Baerlocher and L.B. McCusker. Database of zeolite structures, 1996.

[14] M.D. Foster and M.M.J. Treacy. A database of hypothetical zeolite structures, 2006.

[15] O. Delgado-Friedrichs. Data structures and algorithms for tilings I. *Theor Comput Sci*, 303:431 – 445, 2003.

[16] S.J. Ramsden, V. Robins, and S.T. Hyde. Three-dimensional Euclidean nets from two-dimensional hyperbolic tilings: kaleidoscopic examples. *Acta Cryst. A*, 65:81–108, 2009.

[17] G. Gurtner and M. Durand. Stiffest elastic networks. *arXiv:0805.4712*, 2008.

[18] T. Varslot, A. Kingston, G. Myers, and A. Sheppard. High-resolution helical cone-beam micro-ct with theoretically-exact reconstruction from experimental data. *Medical Physics*, 38:5459, 2011.

[19] M. Saadatfar, A.P. Sheppard, T.J. Senden, and A.J. Kabla. Mapping forces in a 3d elastic assembly of grains. *Journal of the Mechanics and Physics of Solids*, 2011.

[20] A. Katsevich. Theoretically exact filtered backprojection-type inversion algorithm for spiral ct. *SIAM Journal on Applied Mathematics*, pages 2012–2026, 2002.

[21] R.M. Sok, M.A. Knackstedt, A.P. Sheppard, WV Pinczewski, WB Lindquist, A. Venkatarangan, and L. Paterson. Direct and stochastic generation of network models from tomographic images; effect of topology on residual saturations. *Transport in porous media*, 46(2):345–371, 2002.

[22] E.J. Garboczi, Building, and Fire Research Laboratory (US). *Finite element and finite difference programs for computing the linear electric and elastic properties of digital images of random materials*. Building and Fire Research Laboratory, National Institute of Standards and Technology, 1998.

[23] C.H. Arns, M.A. Knackstedt, W.V. Pinczewski, and E.J. Garboczi. Computation of linear elastic properties from microtomographic images: Methodology and agreement between theory and experiment. *Geophysics*, 67(5):1396–1405, 2002.

[24] M. Saadatfar, CH Arns, MA Knackstedt, and T. Senden. Mechanical and transport properties of polymeric foams derived from 3d images. *Colloids and Surfaces A: Physicochemical and Engineering Aspects*, 263(1):284–289, 2005.

[25] M. Saadatfar, M. Mukherjee, M. Madadi, GE Schröder-Turk, F. Garcia-Moreno, FM Schaller, S. Hutzler, AP Sheppard, J. Banhart, and U. Ramamurty. Structure and deformation correlation of closed-cell aluminium foam subject to uniaxial compression. *Acta Materialia*, 60(8):3604–3615, 2012.

Appendix

Table 3: Edge-1- and edge-2-transitive cubic nets analysed according to the functions in equations (2.4)–(2.7). The expressions should evaluate to $\frac{1}{3}, \frac{1}{5}, 0, 0$ respectively. The two nets that satisfy all four conditions (*sqc38* and *sqc1649*) are marked with an asterisk. e_2 (a_2) refers to a second edge type (and its cross-sectional area), symmetrically distinct from the first (there is a dash if the net is edge-1-transitive). The second edge is as listed in *EPINET* [6] (all nets obtained from *RCSR* [5] are edge-1-transitive.) Summands that depend on a_2 are labelled 'var'. If there is a value for a_2 that satisfies the isotropy condition, it is given in the e_2 column. Negative values are unphysical.

s-net	*RCSR name*	*space gp*	*degree*	e_2 (a_2)	eq. 2.4	eq. 2.5	eq. 2.6	eq. 2.7
-	**srs**	$Ia\bar{3}d$	3	-	$\frac{1}{3}$	$\frac{1}{6}$	0	$\neq 0$
*sqc*1	**pcu**	$Im\bar{3}m$	6	-	$\frac{1}{3}$	$\frac{1}{3}$	0	0
*sqc*3	**bcu**	$Im\bar{3}m$	8	-	$\frac{1}{3}$	$\frac{1}{9}$	0	0
*sqc*6	**dia**	$Fd\bar{3}m$	4	-	$\frac{1}{3}$	$\frac{1}{9}$	0	$\neq 0$
*sqc*19	**fcu**	$Fm\bar{3}m$	12	-	$\frac{1}{3}$	$\frac{1}{6}$	0	0
*sqc*35	**nbo**	$Im\bar{3}m$	4	-	$\frac{1}{3}$	$\frac{1}{3}$	0	0
* *sqc*38	**sod-d**	$Im\bar{3}m$	14	0.7698	$\frac{1}{3}$	$\frac{1}{5}$	0	0
*sqc*877	**reo**	$Pm\bar{3}m$	8	-	$\frac{1}{3}$	$\frac{1}{6}$	0	0
*sqc*889	**crs**	$Fd\bar{3}m$	6	-	$\frac{1}{3}$	$\frac{1}{6}$	0	0
*sqc*947	**hxg**	$Pn\bar{3}m$	6	-	$\frac{1}{3}$	$\frac{1}{6}$	0	0
*sqc*970	**sod**	$Im\bar{3}m$	4	-	$\frac{1}{3}$	$\frac{1}{6}$	0	$\neq 0$
*sqc*1568	**cab**	$Pm\bar{3}m$	5	1	$\frac{1}{3}$	var.	0	$\neq 0$
*sqc*2201	**pcb**	$Im\bar{3}m$	4	4.5	$\frac{1}{3}$	var.	0	$\neq 0$
*sqc*3059	**nbo-a**	$Im\bar{3}m$	3	0.5	$\frac{1}{3}$	var.	0	$\neq 0$
*sqc*4991	**bcs**	$Ia\bar{3}d$	6	-	$\frac{1}{3}$	$\frac{1}{9}$	0	0
*sqc*5117	**lcx**	$Pm\bar{3}n$	8	-	$\frac{1}{3}$	$\frac{1}{6}$	0	$\neq 0$
*sqc*5544	**rhr**	$Im\bar{3}m$	4	-	$\frac{1}{3}$	$\frac{1}{9}$	0	$\cong 0$
*sqc*5579	**lcs**	$Ia\bar{3}d$	4	-	$\frac{1}{3}$	$\frac{1}{6}$	0	$\neq 0$
*sqc*7309	**ubt**	$Fm\bar{3}m$	5	-2.29	$\frac{1}{3}$	var.	0	$\neq 0$
*sqc*8843		$Fd\bar{3}m$	9		$\frac{1}{3}$	$\frac{1}{6}$	0	$\neq 0$
*sqc*8990	**reo-e**	$Fm\bar{3}m$	6	0.5	$\frac{1}{3}$	var.	0	$\neq 0$
*sqc*9254	**sod-f**	$Im\bar{3}m$	3		$\frac{1}{3}$	$\frac{1}{6}$	0	$\neq 0$
*sqc*9265	**pcu-f**	$Im\bar{3}m$	3	0.75	$\frac{1}{3}$	var.	0	$\neq 0$
*sqc*9270	**crs-f**	$Fd\bar{3}m$	3	0.125	$\frac{1}{3}$	var.	0	$\neq 0$
*sqc*9271	**pbz**	$Pn\bar{3}m$	3		$\frac{1}{3}$	$\frac{1}{6}$	0	$\neq 0$
*sqc*10956	**pyc**	$Fd\bar{3}m$	8	1.963	$\frac{1}{3}$	var.	0	$\neq 0$
*sqc*11143	**hbo**	$Pm\bar{3}n$	4	0.25	$\frac{1}{3}$	var.	0	$\neq 0$
*sqc*11146	**4/3/c9**	$Fd\bar{3}m$	4		$\frac{1}{3}$	$\frac{1}{6}$	0	$\neq 0$
*sqc*11213	**uks**	$Pn\bar{3}m$	4	-1.09	$\frac{1}{3}$	var.	0	$\neq 0$
*sqc*11215	**rho**	$Im\bar{3}m$	4	1	$\frac{1}{3}$	$\frac{1}{3}$	0	0
*sqc*11218	**ana**	$Ia\bar{3}d$	4	-	$\frac{1}{3}$	.238	0	$\neq 0$
*sqc*12878	**lcs-f**	$Ia\bar{3}d$	3	0.611	$\frac{1}{3}$	var.	0	$\neq 0$
*sqc*12886	**pbg**	$Ia\bar{3}d$	3	0.409	$\frac{1}{3}$	var.	0	$\neq 0$
*sqc*13520	**gie**	$Ia\bar{3}d$	4	-1.23	$\frac{1}{3}$	var.	0	$\neq 0$
* *sqc*1649		$Ia\bar{3}$	8	2.6	$\frac{1}{3}$	var.	0	0
*sqc*2181	**gsi**	$Ia\bar{3}$	4	-0.19	$\frac{1}{3}$	var.	$\neq 0$	$\neq 0$
*sqc*9266	**pcu-g**	$Ia\bar{3}$	3	0.64	$\frac{1}{3}$	var.	$\neq 0$	$\neq 0$
-	**lcv**	$I4_132$	4	-	$\frac{1}{3}$	$\frac{1}{6}$	0	$\neq 0$
-	**lcy**	$P4_132$	6	-	$\frac{1}{3}$	$\frac{1}{6}$	0	$\neq 0$
-	**lcz**	$P4_132$	12	-	$\frac{1}{3}$	$\frac{1}{6}$	0	$\neq 0$
*sqc*2580		$I432$	9	5.66	$\frac{1}{3}$	var.	0	$\neq 0$
*sqc*2969		$P4_232$	6	0.612	$\frac{1}{3}$	var.	0	$\neq 0$
*sqc*3050	**utb**	$I432$	3	-0.39	$\frac{1}{3}$	var.	0	$\neq 0$
*sqc*5115		$I432$	8	-1.73	$\frac{1}{3}$	var.	0	$\neq 0$
*sqc*5523	**unw**	$I432$	4	-1.0	$\frac{1}{3}$	$\frac{1}{3}$	0	$\neq 0$
*sqc*9035		$I4_132$	6		$\frac{1}{3}$	$\frac{1}{6}$	0	$\neq 0$
*sqc*5052	**thp**	$I\bar{4}3d$	8	-	$\frac{1}{3}$	$\frac{1}{6}$	0	$\neq 0$
*sqc*5504	**4/3/c7**	$P\bar{4}3m$	4		$\frac{1}{3}$	$\frac{1}{6}$	0	0
*sqc*11142	**ulj**	$I\bar{4}3d$	4	-0.393	$\frac{1}{3}$	var.	0	$\neq 0$

Table 4: Listing of vertex-2, edge-1-transitive cubic nets analysed for isotropy and mechanical equilibrium according to eqs (2.4)–(2.7). The expressions should evaluate to $\frac{1}{3}, \frac{1}{5}, 0, 0$ respectively if the nets are isotropic. The vertex ordering is as listed in *EPINET* or *RCSR* databases [6, 5].

s-net	*RCSR name*	*space gp*	*degree*	eq. 2.4	eq. 2.5	eq. 2.6	eq. 2.7
sqc169	**flu**	$Fm\bar{3}m$		$\frac{1}{3}$	$\frac{1}{9}$	0	
	vertx 1		4				$\neq 0$
	vertx 2		8				0
sqc867	**ftw**	$Pm\bar{3}m$		$\frac{1}{3}$	$\frac{1}{6}$	0	
	vertx 1		12				0
	vertx 2		12				0
sqc5432	**she**	$Im\bar{3}m$		$\frac{1}{3}$	$\frac{1}{6}$	0	
	vertx 1		4				0
	vertx 2		6				0
sqc5433	**toc**	$Pn\bar{3}m$		$\frac{1}{3}$	$\frac{1}{9}$	0	
	vertx 1		4				0
	vertx 2		6				$\neq 0$
sqc5591	**pto**	$Pm\bar{3}n$		$\frac{1}{3}$	$\frac{1}{6}$	0	
	vertx 1		3				0
	vertx 2		4				$\neq 0$
sqc11070	**gar**	$Ia\bar{3}d$		$\frac{1}{3}$	.227	0	
	vertx 1		4				0
	vertx 2		6				$\neq 0$
-	**iac**	$Ia\bar{3}d$		$\frac{1}{3}$	.227	0	
	vertx 1		4				$\neq 0$
	vertx 2		6				0
-	**ibd**	$Ia\bar{3}d$		$\frac{1}{3}$	$\frac{1}{6}$	0	
	vertx 1		4				$\neq 0$
	vertx 2		6				$\neq 0$
-	**ith**	$Pm\bar{3}n$		$\frac{1}{3}$	.227	0	
	vertx 1		4				$\neq 0$
	vertx 2		12				0
-	**mgc**	$Fd\bar{3}m$		$\frac{1}{3}$	.229	0	
	vertx 1		6				0
	vertx 2		12				$\neq 0$
-	**ocu**	$Im\bar{3}m$		$\frac{1}{3}$	$\frac{1}{9}$	0	
	vertx 1		6				0
	vertx 2		8				0
-	**rht**	$Fm\bar{3}m$		$\frac{1}{3}$	$\frac{1}{6}$	0	
	vertx 1		24				0
	vertx 2		3				$\neq 0$
-	**soc**	$Im\bar{3}m$		$\frac{1}{3}$	$\frac{1}{6}$	0	
	vertx 1		4				0
	vertx 2		6				0
-	**spn**	$Fd\bar{3}m$		$\frac{1}{3}$	.144	0	
	vertx 1		3				$\neq 0$
	vertx 2		6				0
-	**spn-z**	$Fd\bar{3}m$		$\frac{1}{3}$	$\frac{1}{3}$	0	
	vertx 1		3				$\neq 0$
	vertx 2		6				0
-	**tbo**	$Fm\bar{3}m$		$\frac{1}{3}$	$\frac{1}{6}$	0	
	vertx 1		3				$\neq 0$
	vertx 2		4				0
-	**the**	$Pm\bar{3}m$		$\frac{1}{3}$	$\frac{1}{6}$	≈ 0	
	vertx 1		3				$\neq 0$
	vertx 2		8				0
-	**twf**	$Im\bar{3}m$		$\frac{1}{3}$	.227	0	
	vertx 1		3				$\neq 0$
	vertx 2		8				0
-	**pyr**	$Pa\bar{3}$		$\frac{1}{3}$	$\frac{1}{6}$	0	
	vertx 1		3				$\neq 0$
	vertx 2		6				0
-	**cys**	$P4_232$		$\frac{1}{3}$	0.228	0	
	vertx 1		3				$\neq 0$
	vertx 2		4				0
-	**ifi**	$I4_132$		$\frac{1}{3}$	$\frac{1}{6}$	0	
	vertx 1		4				$\neq 0$
	vertx 2		6				≈ 0
-	**ssc**	$I4_132$		$\frac{1}{3}$	$\frac{1}{6}$	0	
	vertx 1		4				$\neq 0$
	vertx 2		6				$\neq 0$
sqc975	**bor**	$P\bar{4}3m$		$\frac{1}{3}$	$\frac{1}{6}$	0	
	vertx 1		3				$\neq 0$
	vertx 2		4				$\neq 0$
sqc5593	**ctn**	$I\bar{4}3d$		$\frac{1}{3}$	$\frac{1}{6}$	0	
	vertx 1		3				$\neq 0$
	vertx 2		4				≈ 0
-	**ttt**	$F\bar{4}3m$		$\frac{1}{3}$	$\frac{1}{6}$	0	
	vertx 1		3				$\neq 0$
	vertx 2		12				$\neq 0$